Journal of Colloid and Interface Science 728 (2027) 141794

Contents lists available at ScienceDirect

Journal of Colloid And Interface Science

journal homepage: www.elsevier.com/locate/jcis

Bidentate-chelated nickel complex orchestrates S-scheme heterojunction on CdZnS for robust noble-metal-free photocatalytic hydrogen evolution

Yifan Liao, Jiayi Meng, Quanmei Zhou, Yuchen Wei, Yuying Hu, Mohan Zhang, Yakun Song, Bite Deng, Hongyan Zhao, Wei-Lin Dai *

State Key Laboratory of Porous Materials for Separation and Conversion, Shanghai Key Laboratory of Molecular Catalysis and Innovative Materials, Department of Chemistry, Fudan University, Shanghai, 200438, PR China

HIGHLIGHTS

- A novel $Cd_{0.3}Zn_{0.7}S/[Ni(en)_3]S_2O_3$ S-scheme heterojunction was constructed.
- The bidentate-chelated Ni complex acts as an intrinsic interfacial electronic unit.
- The optimized 3-CZS/NES achieves an H_2 evolution rate of 46.53 $mmol \cdot g^{-1} \cdot h^{-1}$.
- The catalyst outperforms pristine CZS and 1 wt% Pt-loaded CZS.
- ISI-XPS, fs-TAS, and DFT reveal the S-scheme electron transfer mechanism.

GRAPHICAL ABSTRACT

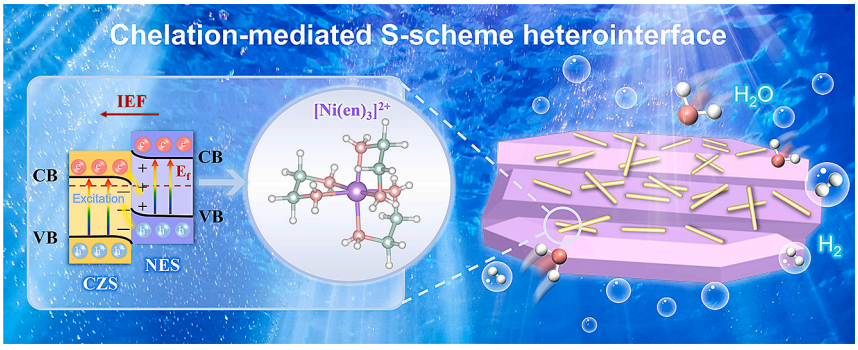

ARTICLE INFO

Keywords:
Bidentate-chelated nickel complex
S-scheme heterojunction
Interfacial electronic engineering
Charge transfer dynamics
Photocatalytic hydrogen evolution

ABSTRACT

Noble-metal-free photocatalysts that combine high activity with long-term durability remain scarce for solar hydrogen production. Transition-metal coordination complexes possess highly tunable electronic structures and chelation-stabilized configurations, yet their use as intrinsic interfacial components for regulating charge dynamics remains underexplored. Herein, an S-scheme $Cd_{0.3}Zn_{0.7}S/[Ni(en)_3]S_2O_3$ heterojunction was constructed through an in situ solvothermal strategy, in which the bidentate-chelated octahedral Ni complex $[Ni(en)_3]S_2O_3$ acts as an interfacial electronic modulator. The optimized $Cd_{0.3}Zn_{0.7}S/[Ni(en)_3]S_2O_3$ photocatalyst delivered an H_2 evolution rate of 46.53 $mmol \cdot g^{-1} \cdot h^{-1}$ under visible light irradiation, 3.3 times that of $Cd_{0.3}Zn_{0.7}S$ and higher than that of 1 wt% Pt-loaded $Cd_{0.3}Zn_{0.7}S$. It also exhibited enhanced photostability and an apparent quantum efficiency of 18.6% at 350 nm. In situ irradiated X-ray photoelectron spectroscopy (ISI-XPS), femtosecond transient absorption spectroscopy (fs-TAS) and density functional theory (DFT) calculations revealed that the robust heterointerface induces spontaneous electron migration from $[Ni(en)_3]S_2O_3$ to $Cd_{0.3}Zn_{0.7}S$, establishing interfacial band bending and a built-in electric field for S-scheme charge transfer. This work demonstrates that chelation-stabilized complexes can serve as effective electronic regulators at semiconductor interfaces, providing a versatile strategy for constructing active, stable, and noble-metal-free photocatalysts for solar hydrogen production.

* Corresponding author.
E-mail address: wldai@fudan.edu.cn (W.-L. Dai).

https://doi.org/10.1016/j.jcis.2026.141794
Received 28 July 2026; Received in revised form 9 October 2026; Accepted 11 October 2026
Available online 12 October 2026
0021-9797/© 2026 Elsevier Inc. All rights are reserved, including those for text and data mining, AI training, and similar technologies.

1. Introduction

Fossil resources remain central to the current energy system, yet their extensive consumption results in substantial carbon emissions and growing environmental pressure. Hydrogen (H_2) is therefore regarded as a promising alternative energy carrier because of its high mass-specific energy density and carbon-free end use. In this context, solar-driven photocatalytic H_2 evolution provides a sustainable and promising pathway for converting renewable solar energy into chemical energy, contributing to a carbon-neutral future [1–4].

Among numerous photocatalytic semiconductor candidates, metal sulfides—particularly the $Cd_xZn_{1-x}S$ solid solutions—have attracted considerable attention because their composition-dependent electronic structures enable favorable carrier transport and provide numerous surface reaction sites [5–7]. Nevertheless, pristine $Cd_xZn_{1-x}S$ suffers from substantial carrier loss due to rapid recombination of photogenerated electrons and holes, resulting in poor utilization of photogenerated charge carriers. Moreover, the severe photocorrosion arising from the self-oxidation of lattice sulfide anions (S^{2-}) by accumulated holes further compromises both catalytic activity and structural stability [8–10]. Despite the widespread use of Pt and Au as cocatalysts for promoting charge-carrier separation [11–13], the scarcity and high cost of noble metals, together with potential agglomeration-induced deactivation, hinder their scalability for industrial applications [14,15]. Consequently, developing earth-abundant alternatives and constructing rational heterojunctions, especially S-scheme architectures, have emerged as important research directions [16–18]. Such architectures exploit the interfacial built-in electric field (IEF) to drive directional carrier migration while preserving carriers with strong redox capability, thereby suppressing charge recombination and photocorrosion through interfacial electronic regulation [19–22].

Nickel (Ni), characterized by its unique $3d^84s^2$ electronic configuration, exhibits multiple accessible oxidation states ranging from Ni(0) to Ni(IV) [23,24]. This flexible multivalent capability endows nickel-based materials with exceptional potential for electron transfer, enabling them to efficiently mediate complex catalytic cycles. Moreover, the electronic structure of nickel centers displays pronounced ligand-field sensitivity [25–27]. Through the rational design of organic ligands, the electron density and coordination environment of nickel centers can be precisely tuned, thereby optimizing their physicochemical properties and catalytic efficiency. Particularly, polydentate ligands can generate strong chelation effects, enhancing the thermodynamic stability and structural rigidity of nickel coordination complexes during prolonged catalysis, which has contributed to their broad application in catalytic reactions [28–30]. In the realm of photocatalytic hydrogen evolution, nickel-based catalysts are distinguished by their low proton reduction overpotentials and rapid surface reaction kinetics. Furthermore, the natural abundance and relatively low cost of Ni favor its use in sustainable catalyst design compared with noble-metal counterparts. Within the family of Ni coordination compounds, $[Ni(en)_3]S_2O_3$ stands out due to its facile synthesis and robust structural integrity. In this complex, three bidentate ethylenediamine (en) ligands coordinate with the nickel center to form a stable octahedral chelate framework. This rigid architecture effectively suppresses ligand dissociation and metal agglomeration under reactive conditions, enabling the complex to exhibit superior activity in electrocatalytic hydrogen production [31]. Given its exceptional structural stability and favorable electron-transfer properties, systematic investigation of its photocatalytic performance is highly warranted. More importantly, coupling $[Ni(en)_3]S_2O_3$ with $Cd_xZn_{1-x}S$ presents a compelling opportunity to establish an S-scheme heterointerface capable of improving carrier utilization and catalytic performance.

In this work, we successfully constructed the $Cd_{0.3}Zn_{0.7}S/[Ni(en)_3]S_2O_3$ (CZS/NES) S-scheme heterojunction via a facile in situ solvothermal strategy. To our knowledge, $[Ni(en)_3]S_2O_3$ (NES) has not previously been employed as an interfacial functional component for electronic regulation of photocatalytic hydrogen evolution. The optimized 3-CZS/NES composite exhibits exceptional photocatalytic activity, delivering a hydrogen production rate of 46.53 $mmol \cdot g^{-1} \cdot h^{-1}$ under visible-light illumination. This value is 3.3-fold higher than that of pristine $Cd_{0.3}Zn_{0.7}S$ (CZS) and the catalyst also exhibits improved cycling stability. The substantial activity enhancement mainly originates from interfacial regulation enabled by the S-scheme heterostructure. The IEF formed across the heterointerface effectively promotes the spatial separation and directional migration of charge carriers while inhibiting electron–hole recombination. Furthermore, the ultrafast carrier dynamics and the underlying S-scheme charge transfer mechanism during the photocatalytic hydrogen evolution reaction were elucidated through advanced characterization techniques, including in situ irradiated X-ray photoelectron spectroscopy (ISI-XPS) and femtosecond transient absorption spectroscopy (fs-TAS). This work not only demonstrates the potential of nickel coordination complexes in photocatalysis but also provides an innovative strategy for the design of efficient and noble-metal-free S-scheme photocatalysts.

2. Materials and methods

2.1. Materials

Zinc acetate dihydrate ($Zn(CH_3COO)_2 \cdot 2H_2O$, $\geq$ 99.0%), thiourea (CH_4N_2S, $\geq$ 99.0%), ethylenediamine ($C_2H_8N_2$, $\geq$ 99.0%), sodium thiosulfate pentahydrate ($Na_2S_2O_3 \cdot 5H_2O$, $\geq$ 99.0%), sodium sulfide nonahydrate ($Na_2S \cdot 9H_2O$, $\geq$ 98.0%), sodium sulfite (Na_2SO_3, $\geq$ 97.0%) were supplied by Sinopharm Chemical Reagent Co., Ltd. Cadmium acetate dihydrate ($Cd(CH_3COO)_2 \cdot 2H_2O$, 99.5%) was sourced from Shanghai Macklin Biochemical Technology Co., Ltd. Nickel(II) chloride anhydrous ($NiCl_2$, > 98.0%) was purchased from Tokyo Chemical Industry Co., Ltd. Deionized water and analytical-grade ethanol (C_2H_5OH) were directly employed in all experiments.

2.2. Preparation of photocatalysts

Synthesis of $Cd_{0.3}Zn_{0.7}S$. Typically, $Cd(CH_3COO)_2 \cdot 2H_2O$ (0.6 mmol), $Zn(CH_3COO)_2 \cdot 2H_2O$ (1.4 mmol), and thiourea (6.0 mmol) were sequentially added into 72 mL of an ethylenediamine/deionized water mixture (2:1, *v*/v) under magnetic stirring. After 20 min, the resulting precursor solution was transferred to a 100 mL Teflon-lined stainless-steel autoclave and heated at 180 °C for 12 h. The yellow solid was successively rinsed three times with deionized water and ethanol and dried under vacuum at 60 °C overnight to yield the $Cd_{0.3}Zn_{0.7}S$ sample, which was denoted as CZS.

Synthesis of $[Ni(en)_3]S_2O_3$. Following a previously reported method [31], an aqueous solution containing 3 mmol of $NiCl_2$ and 3 mmol of $Na_2S_2O_3 \cdot 5H_2O$ was prepared in 40 mL of deionized water, followed by the dropwise addition of 2 mL of ethylenediamine. After an additional 1 h of stirring, the precipitate was isolated, washed and dried overnight at 70 °C to afford $[Ni(en)_3]S_2O_3$, abbreviated as NES.

Synthesis of $Cd_{0.3}Zn_{0.7}S/[Ni(en)_3]S_2O_3$. Similar to the preparation of pristine CZS, a desired amount of NES was first dispersed in 72 mL of an ethylenediamine/deionized water mixture (2:1, *v*/v) under magnetic stirring for 30 min. $Cd(CH_3COO)_2 \cdot 2H_2O$ (0.6 mmol), $Zn(CH_3COO)_2 \cdot 2H_2O$ (1.4 mmol), and thiourea (6.0 mmol) were then added sequentially, followed by stirring for another 30 min to ensure uniform mixing. The suspension was then transferred to a 100 mL Teflon-lined autoclave for solvothermal treatment at 180 °C for 12 h. The resultant precipitate was recovered by centrifugation, washed and vacuum-dried at 60 °C overnight to yield the final $Cd_{0.3}Zn_{0.7}S/[Ni(en)_3]S_2O_3$ composites. Depending on the initial feed mass of NES (20, 50, 60, 70, and 100 mg), the products were labeled as x-CZS/NES (x = 1, 2, 3, 4, and 5, respectively).

2.3. Characterization

The morphologies and microstructures of the samples were observed with scanning electron microscopy (SEM, Zeiss Gemini 300, Germany) and field emission transmission electron microscopy (TEM, Tecnai G2 F20 STwin, FEI). Phase identification was performed by X-ray diffraction (XRD, D8 PHASER, Bruker Corp., Germany). Fourier-transform infrared (FTIR) spectra were recorded on a Nicolet iS10 spectrometer (Thermo Fisher Scientific). Nitrogen adsorption–desorption measurements were conducted at 77 K using a Micromeritics TriStar 3020 analyzer to determine the specific surface area (S_{BET}) and pore-size distribution. The surface elemental composition and chemical states of the photocatalysts were examined by X-ray photoelectron spectroscopy (XPS, AXIS Supra+, Kratos Analytical Inc.). In situ irradiated XPS measurements were performed using an AXIS Supra+ instrument equipped with a tunable wavelength laser manufactured by Ningbo Laser Technology Co., Ltd., China, using the power supply model LSR-PS-II5, with an S-400 μm-S-1 M fiber. Ultraviolet photoelectron spectroscopy (UPS) measurements were carried out using an unfiltered He discharge source with a photon energy of 21.22 eV. The Fermi level was referenced to a clean Au surface after Ar-ion sputtering, which was set to 0 eV. The optical absorption characteristics of the samples were examined by an ultraviolet–visible diffuse reflectance spectrometer (UV–Vis DRS) (Lambda 650S, PE Corp., America). Steady-state photoluminescence (PL) and time-resolved photoluminescence (TRPL) measurements were conducted on an Edinburgh FLS1000 fluorescence spectrometer with an excitation wavelength of 380 nm. Thermogravimetric analysis (TGA) was carried out using a HITACHI STA200 simultaneous thermal analyzer under an N_2 atmosphere, with the temperature increased from room temperature to 800 °C at a heating rate of 15 °C/min. Electron paramagnetic resonance (EPR) measurements were performed using a Bruker EMXplus-6/1 spectrometer.

2.4. Photoelectrochemical test

All photoelectrochemical measurements were performed on a Chenhua CHI760E workstation in a standard three-electrode cell, in which the catalyst-coated fluorine-doped tin oxide (FTO) substrate, a Pt plate, and a saturated calomel electrode (SCE) acted as the working, counter, and reference electrodes, respectively. For photoelectrode fabrication, 2 mg of photocatalyst powder was added to a mixture of 2 mL ethanol and 10 μL Nafion followed by ultrasonication for 30 min. Then the catalyst was dripped onto the FTO glass. The transient photocurrent response curves were measured in a 0.5 M Na_2SO_4 electrolyte under illumination from a 300 W Xe lamp. Mott–Schottky curves were recorded over a potential window of −1.0 to 0.2 V at frequencies of 0.2, 0.5, and 1.0 kHz. To estimate the electrochemically active surface area (ECSA), cyclic voltammetry (CV) was carried out in the non-Faradaic region between 0.20 and 0.30 V vs. SCE at scan rates ranging from 20 to 140 $mV{\cdot}s^{-1}$. The current density difference between the anodic and cathodic branches at 0.25 V was plotted as $\Delta J/2$ against scan rate. The slope of the resulting linear fit was taken as C_{dl}, which was used to comparatively assess the relative ECSA of the samples. Electrochemical impedance spectroscopy (EIS) measurements were carried out at the open circuit potential using an electrolyte containing 0.025 M potassium ferricyanide and 0.1 M KCl. The frequency was swept from 100 kHz to 0.01 Hz.

2.5. Photocatalytic hydrogen evolution measurement

Photocatalytic hydrogen evolution (PHE) measurements were performed in a sealed gas-circulation system. Illumination was provided by a 300 W Xe lamp (Perfect Light, Beijing, China) fitted with a 420 nm cutoff filter. The reaction system was kept at 20 °C by continuous water circulation. The incident light power density at the reactor surface and the effective illuminated area were 1464.5 $W{\cdot}m^{-2}$ and 41.85 cm^2, respectively. Typically, 10 mg of photocatalyst was suspended in 100 mL of an aqueous solution containing 0.35 M $Na_2S{\cdot}9H_2O$ and 0.25 M Na_2SO_3 as sacrificial agents. The resulting suspension was introduced into the photoreactor, followed by evacuation to eliminate residual air before illumination. The evolved H_2 was quantified using a gas chromatograph equipped with a 5 Å molecular sieve column and a thermal conductivity detector (TCD). Quantitative analysis was performed by external calibration using a certified 5 vol% H_2/Ar standard gas mixture. A series of known amounts of H_2 were successively injected to construct a calibration curve relating chromatographic peak area to H_2 content. The apparent quantum efficiencies (AQEs) for H_2 evolution were evaluated under monochromatic irradiation at 350, 400, 420, 450 and 500 nm according to the following equation:

$$\mathrm{AQE}\left(\%\right) = \frac{\text{number of reacted electrons}}{\text{number of incident photons}} \times 100\%$$

$$= \frac{\text{number of evolved } H_2 \text{ molecules} \times 2}{\text{number of incident photons}} \times 100\%$$

2.6. Femtosecond transient absorption spectroscopy (fs-TAS)

The fs-TAS measurements were performed using a Ti:sapphire laser regenerative amplifier (Astrella, Coherent; 800 nm, 100 fs, 1 kHz). Pump pulses at 380 nm were generated by an optical parametric amplifier (OPerA Solo, Coherent), while a broadband white-light continuum served as the probe. Transient spectra were recorded with a Helios spectrometer (Ultrafast Systems). The pump frequency was reduced to 500 Hz using an optical chopper, and its polarization was adjusted to 54.7° relative to the probe. Samples were measured in a 2 mm fused-silica cuvette.

2.7. Density functional theory (DFT) calculations

DFT calculations were carried out with Vienna Ab initio Simulation Package (VASP) [32]. The Perdew–Burke–Ernzerhof (PBE) [33] functional, supplemented by the D3(BJ) dispersion correction [34], was adopted. Core–valence interactions were treated using the projector augmented-wave (PAW) approach [35], and the plane-wave cutoff energy was fixed at 500 eV. For hydrogen evolution reaction calculations, a 3×2 supercell of the Cd-doped ZnS (001) surface and a $\sqrt{3} \times 1$ supercell of $[Ni(en)_3]S_2O_3$ (001) were constructed. The CZS/NES heterostructure was constructed by coupling the CZS (001) surface with the NES (001) surface to form a CZS(001)/NES(001) interfacial configuration, with a vacuum gap of ≈25 Å separating periodic slabs. A Monkhorst-Pack k-point mesh [36] with a density of 0.07 $Å^{-1}$ was adopted with a Gaussian smearing [37] of 0.1 eV. The wavefunctions were fully relaxed until the change in electronic energy and the change in eigenvalues were both below 10^{-6} eV. The structures were fully relaxed until the maximum force on each atom was less than 0.02 eV/Å. The work function Φ was determined according to the following equation:

$$\Phi = E_{vac} - E_{Fermi}$$

where E_{vac} and E_{Fermi} represent the vacuum level and the Fermi level, respectively.

3. Results and discussion

3.1. Morphology and structure characterization

Fig. 1a illustrates the fabrication of the CZS/NES composite. Briefly, NES was first obtained via a facile coordination-precipitation reaction, and CZS was subsequently nucleated and grown directly on the NES surface during the solvothermal step to afford the CZS/NES heterostructure. The morphology and microstructure of CZS, NES and CZS/

NES were characterized by SEM and TEM. Pristine CZS displays a morphology composed of aggregated nanorods (Fig. S1a–d). High-resolution transmission electron microscopy (HRTEM) analysis (Fig. S1e) reveals clear lattice fringes with an interplanar spacing of 0.32 nm, corresponding to the (002) plane of CZS [10,38]. Moreover, the corresponding energy-dispersive X-ray spectroscopy (EDS) elemental mapping images (Fig. S1f–i) further verify that Cd, Zn, and S are evenly distributed along the nanorods. The microscopic morphological features of pristine NES are shown in Fig. 1b and Fig. S2. The SEM and TEM images reveal that NES possesses a well-defined, dense, and monolithic micrometer-sized prismatic architecture with a smooth surface and sharp geometric facets, which indicate its high crystallinity and robust structural stability. After coupling with CZS, both SEM and TEM images (Fig. 1c,d) show that CZS nanorods are uniformly anchored on the NES microprisms, forming a hierarchically integrated CZS/NES composite. This intimate decoration suggests close interfacial contact achieved through the in situ growth strategy. To further probe the interfacial characteristics at the atomic level, HRTEM was employed. As shown in Fig. 1e, a coherent and intimate heterojunction interface is formed between CZS and NES. HRTEM reveals a 0.32 nm lattice periodicity at the CZS/NES interface, assignable to the (002) plane of CZS. Notably, due to the substantial thickness of the NES microprisms, the electron beam penetration is intrinsically restricted, resulting in an electron-opaque contrast that precludes the resolution of clear lattice fringes for the NES phase under HRTEM conditions [39]. Nevertheless, this was complemented by high-angle annular dark-field scanning transmission electron microscopy (HAADF-STEM) and EDS mappings (Fig. 1f). The results demonstrate a homogeneous distribution and clear spatial overlap of C, N, O, S, Ni, Zn, and Cd across the composite architecture, which collectively support the successful construction of a closely contacted CZS/NES heterojunction.

The crystalline phase and structural characteristics of the samples were examined by XRD. As illustrated in Fig. 2a, CZS displays a diffraction profile characteristic of a hexagonal wurtzite structure [40]. Notably, the diffraction peaks of CZS lie between the reference patterns of hexagonal CdS (PDF#77–2306) and ZnS (PDF#36–1450). This distinct shift toward higher angles relative to pure CdS clearly indicates the formation of a Cd—Zn solid solution. Such lattice modulation stems from the isomorphous substitution of Cd^{2+} (0.97 Å) by the smaller Zn^{2+} (0.74 Å), which leads to an intrinsic lattice contraction and a subsequent decrease in d-spacing [41]. To elucidate the precise crystal structure of NES, a rigorous Rietveld refinement of the XRD data was performed, as illustrated in Fig. 2b. The refinement results demonstrate an excellent visual agreement between the experimental pattern (red circles) and the calculated pattern (black solid line). The difference curve (grey line at the bottom) remains relatively flat across the entire 2 theta range, indicating that the adopted structural model accurately represents the phase composition of the synthesized complex. The reliability factors for the refinement are $R_{wp} = 15.51\%$, $R_p = 11.35\%$, and a GOF of 3.94. While these values are slightly elevated, they are considered scientifically reasonable given the high structural complexity of the coordination framework and the presence of numerous light atoms (C, N, and H) with relatively low X-ray scattering power. These refinement parameters support the reliability of the structural assignment. Furthermore, the Rietveld refinement results not only corroborate the high crystallinity of NES but also elucidate the local coordination environment of the Ni^{2+} centers. Specifically, the Ni^{2+} ions are tightly chelated by three ethylenediamine ligands, giving rise to a stable octahedral configuration. This

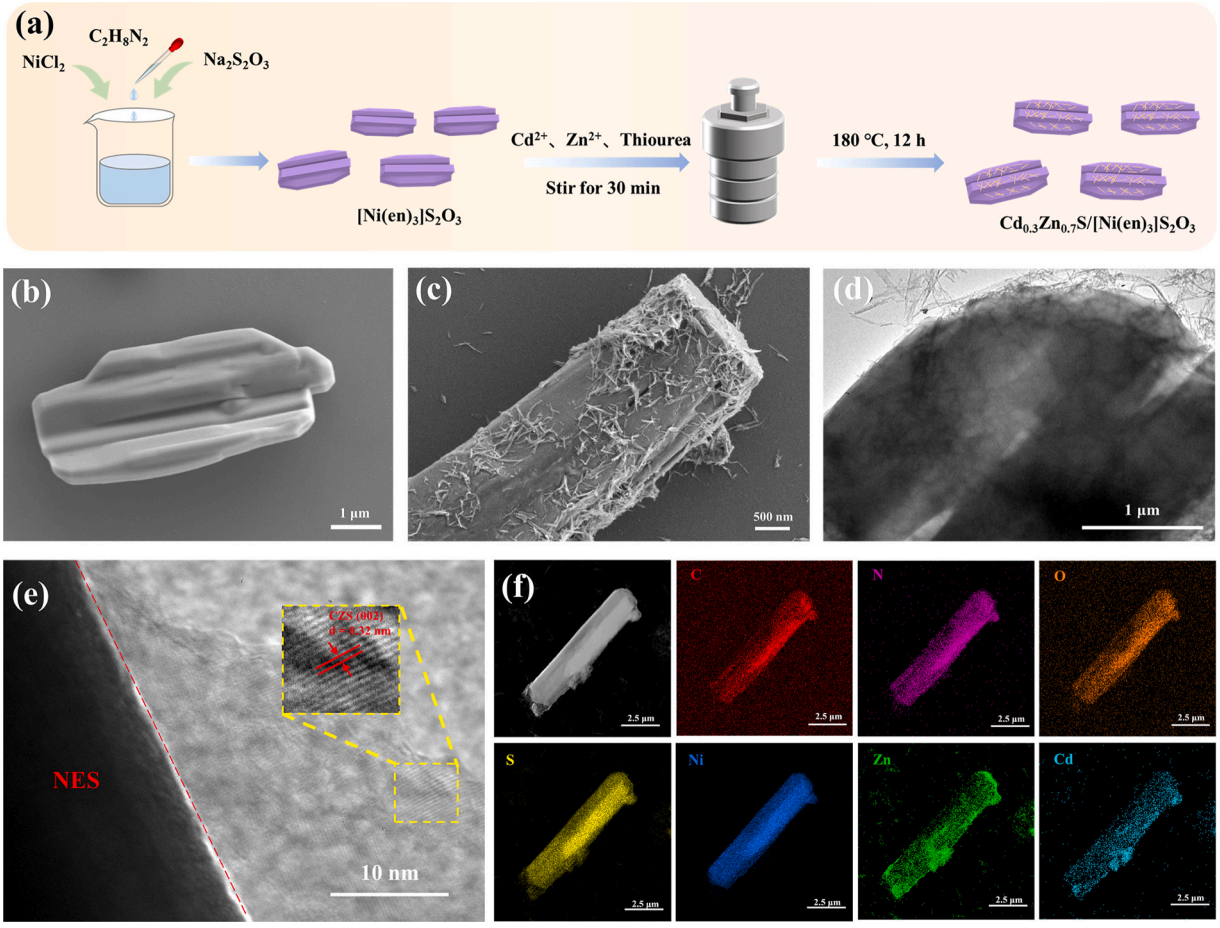

Fig. 1. (a) Schematic illustration of the synthesis of CZS/NES. SEM images of (b) NES and (c) CZS/NES. (d) TEM and (e) HRTEM images of CZS/NES. (f) HAADF-STEM image and EDS elemental mapping images of C, N, O, S, Ni, Zn, and Cd for CZS/NES.

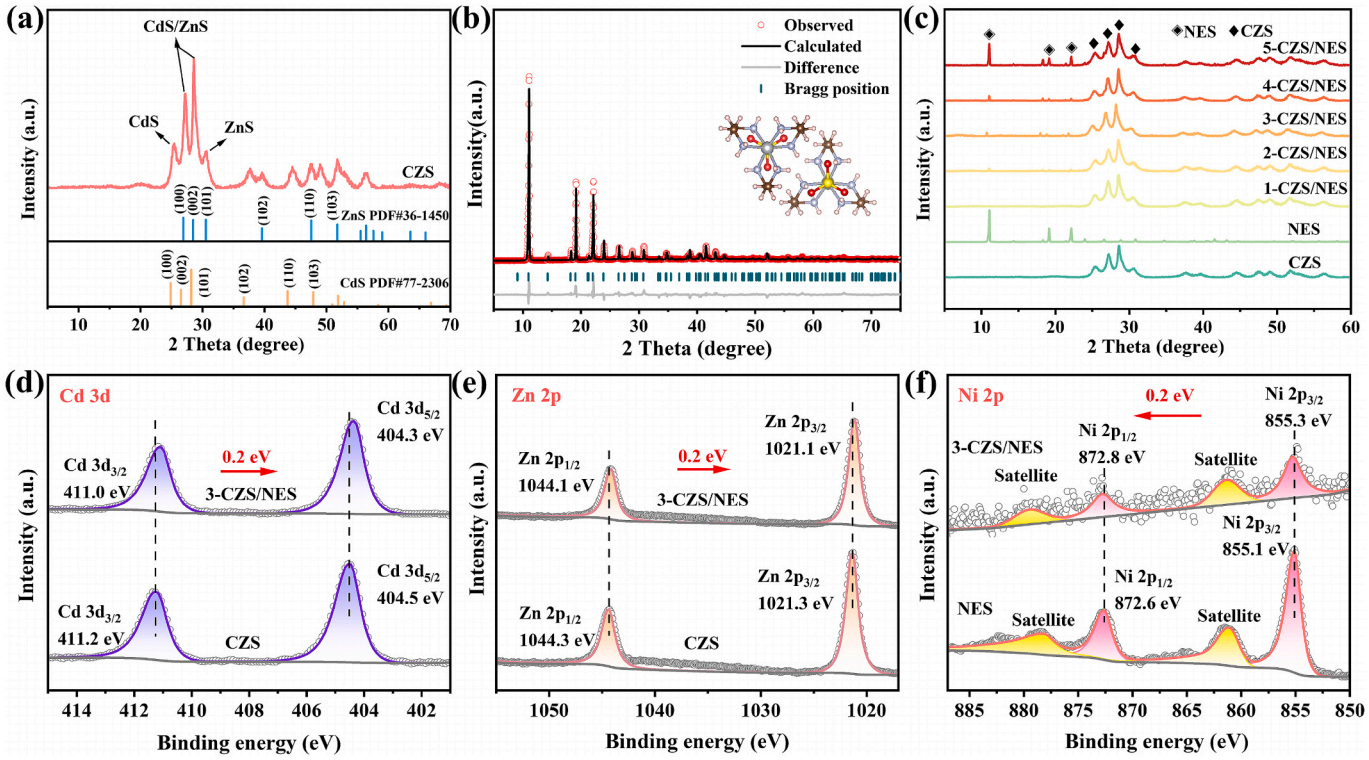

Fig. 2. (a) XRD pattern of CZS together with the reference diffraction patterns of ZnS (PDF#36–1450) and CdS (PDF#77–2306). (b) Rietveld refinement of the XRD pattern of NES. (c) XRD patterns of CZS, NES and x-CZS/NES (x = 1, 2, 3, 4, and 5); the characteristic reflections assigned to CZS and NES are marked accordingly. High-resolution XPS spectra of (d) Cd 3d, (e) Zn 2p and (f) Ni 2p for the corresponding samples.

precise structural model provides a robust crystallographic foundation for interpreting the structural stability and electron transfer mechanism of NES. The XRD profiles of CZS/NES composites prepared with varying component ratios are presented in Fig. 2c. Owing to the higher proportion of CZS, the diffraction profiles of the composites are primarily governed by the characteristic reflections of CZS. Notably, with increasing NES loading, a distinctive diffraction peak at 11.06°—assignable to the (100) plane of NES—gradually emerges and intensifies. This trend clearly confirms the successful incorporation of NES and the formation of well-defined CZS/NES heterostructures. FTIR spectra further corroborate the presence of NES in the composite (Fig. S3). For pristine NES, the broad absorption in the 3200–3400 cm^{-1} region together with the signal at 1583 cm^{-1} originate from N—H stretching and bending vibrations of $–NH_2$ groups, respectively. Absorptions in the 2850–2950 cm^{-1} interval arise from C—H vibrations of the ethylenediamine moieties, while the feature at 527 cm^{-1} is characteristic of Ni—N coordination within the octahedral complex [31,42]. These characteristic NES bands remain visible in the composites, although with reduced intensity because of the lower NES content, indicating that the chelate structure survives the in situ solvothermal process. To quantitatively evaluate the incorporation of NES, inductively coupled plasma optical emission spectroscopy (ICP-OES) analysis was performed on the x-CZS/NES series. As summarized in Table S1, the Ni content increased progressively with increasing initial NES feed. Notably, the optimized 3-CZS/NES sample exhibited an actual Ni content of 1.34 wt%, supporting the successful incorporation of NES. TGA was further performed to examine the incorporation of NES (Fig. S4). Pristine NES exhibited a pronounced mass loss of approximately 76.3%, with a major DTG peak at 276.1 °C, which is associated with thermal decomposition of its organic ligands. In comparison, pristine CZS showed a smaller total mass loss of approximately 9.6% and a characteristic DTG feature at 395.0 °C. The 3-CZS/NES composite exhibited a total mass loss of approximately 12.1% and displayed two DTG peaks at 279.3 and 395.0 °C, corresponding closely to the characteristic thermal decomposition features of NES and CZS, respectively. These thermal features provide further evidence for the incorporation of NES and support the retention of its coordination environment after the solvothermal treatment. The S_{BET} and pore structures of the samples were evaluated by N_2 sorption analysis. Fig. S5 shows that CZS, NES, and 3-CZS/NES all display type-IV adsorption isotherms together with H3-type hysteresis loops, indicative of mesoporous features [43]. Notably, the S_{BET} of the optimized CZS/NES composite is comparable to that of pristine CZS, implying that the improved H_2 evolution performance mainly originates from enhanced interfacial charge separation and transfer rather than from a simple surface-area effect. The surface hydrophilicity was further examined by water contact angle analysis (Fig. S6). Compared with pristine CZS (35.7°), 3-CZS/NES exhibited a lower water contact angle of 31.6°, indicating improved hydrophilicity after NES incorporation. The improved wettability favors more effective interaction between the catalyst surface and the liquid phase, thereby creating more accessible interfacial sites for photocatalytic reactions [44,45].

XPS analysis was further employed to probe the surface composition and interfacial electronic interactions. The survey XPS spectra of the catalysts are presented in Fig. S7. For the 3-CZS/NES composite, characteristic peaks corresponding to Cd, Zn, S, Ni, N, C, and O are simultaneously observed, evidencing the simultaneous presence of both CZS and NES. High-resolution XPS spectra further revealed the electronic interactions at the interface between CZS and NES. For pristine CZS, the Cd 3d spectrum exhibits two peaks centered at 404.5 and 411.2 eV, corresponding to Cd $3d_{5/2}$ and Cd $3d_{3/2}$, respectively (Fig. 2d). The Zn 2p spectrum (Fig. 2e) shows two characteristic signals at 1021.3 and 1044.3 eV, which are associated with Zn $2p_{3/2}$ and Zn $2p_{1/2}$. For NES, the Ni 2p spectrum (Fig. 2f) displays a typical doublet accompanied by satellite peaks. The peaks at 855.1 and 872.6 eV can be attributed to Ni $2p_{3/2}$ and Ni $2p_{1/2}$ of coordinated Ni^{2+} species, respectively [46]. Notably, after the formation of 3-CZS/NES heterojunction, discernible binding-energy shifts are observed. Specifically, the Cd 3d and Zn 2p

signals of CZS shift by 0.2 eV toward lower binding energy, whereas the Ni 2p peaks of NES shift by approximately 0.2 eV toward higher binding energy. Lower binding energy is generally associated with an increase in local electron density, whereas a shift toward higher binding energy is commonly associated with electron depletion [47]. Consequently, these opposite shifts are consistent with interfacial electron redistribution from NES to CZS. The observed interfacial electronic coupling confirms close interfacial contact between CZS and NES and is conducive to the formation of an IEF, thereby promoting spatial charge separation in the S-scheme photocatalytic process.

To further clarify the optical response and band structures of the catalysts, UV–Vis DRS, valence band XPS (VB-XPS), and Mott–Schottky measurements were performed. As illustrated in Fig. 3a, CZS exhibits a characteristic semiconductor absorption profile with an absorption edge near 520 nm. NES reveals a broad absorption band spanning the visible to the long-wavelength region, which can be mainly ascribed to electronic transitions associated with the coordinated Ni species [48]. After coupling with NES, the CZS/NES composites retain the characteristic absorption features of CZS while displaying a red shift of the absorption edge and progressively enhanced long-wavelength absorption with increasing NES content. This result indicates that incorporating NES broadens the spectral response of the heterostructure, thereby providing favorable optical conditions for photocatalytic H_2 evolution. The optical bandgap (E_g) values were estimated from the UV–Vis DRS data using Tauc analysis (Fig. 3b). The E_g value of CZS was estimated to be approximately 2.47 eV, while that of 3-CZS/NES was approximately 2.45 eV. This slight narrowing of the bandgap indicates that coupling with NES alters the electronic structure of CZS and reduces the energy required for electronic transitions. In contrast, the optical absorption profile of NES does not exhibit a clear band-edge feature, presenting instead a broad absorption band that extends across a wide spectral range. This behavior is characteristic of coordination compounds, in which light absorption arises mainly from d–d transitions and charge-transfer transitions, differing from the interband transitions observed in conventional semiconductors. Therefore, determining the bandgap of NES via the Tauc method is not feasible. Accordingly, the band structure of NES was established by combining VB-XPS with Mott–Schottky analysis. Fig. 3c shows that the energy separation between the Fermi level (E_f) and the valence band maximum (VBM) of NES was determined to be 1.39 eV through linear extrapolation of the VB-XPS low-binding-energy edge. Taking the instrument work function ($\Phi_{inst} = 4.5$ eV) into account, the valence band potential (E_{VB}) of NES relative to the normal hydrogen electrode (NHE) was calculated to be 1.45 eV according to $E_{VB,NHE} = \Phi_{inst} + E_{VB,XPS} - 4.44$ eV. Mott–Schottky analysis was subsequently employed to further determine the semiconductor characteristics of the catalysts. Both CZS and NES display positive slopes (Fig. 3d,e), indicating n-type semiconductor behavior [49]. The flat-band potentials (E_{FB}) of CZS and NES were determined to be −0.74 V and − 0.77 V vs. SCE, respectively, corresponding to −0.50 V and − 0.53 V relative to NHE ($E_{NHE} = E_{SCE} + 0.241$ V). Applying the commonly used 0.2 V offset between E_{FB} and conduction band (CB) edge for n-type semiconductors, the conduction band potentials (E_{CB}) of CZS and NES were estimated as −0.70 V and − 0.73 V vs. NHE, respectively. Using the E_g value derived from the aforementioned Tauc plot, the E_{VB} of CZS was determined to be 1.77 V via the relation $E_{VB} = E_{CB} + E_g$. Based on the above results, the band structures of CZS and NES are summarized in Fig. 3f. The E_{CB} values of both components are more negative than the H^+/H_2 reduction potential (0 V vs. NHE), providing sufficient thermodynamic driving force for PHE [50,51]. More importantly, the staggered band alignment is consistent with the S-scheme heterojunction paradigm, providing a favorable band structure foundation for directional charge migration while preserving strong redox capability.

3.2. Photocatalytic hydrogen evolution performance and charge transfer behavior

Photocatalytic hydrogen evolution activity was assessed under visible-light illumination from a 300 W Xe lamp equipped with a 420 nm

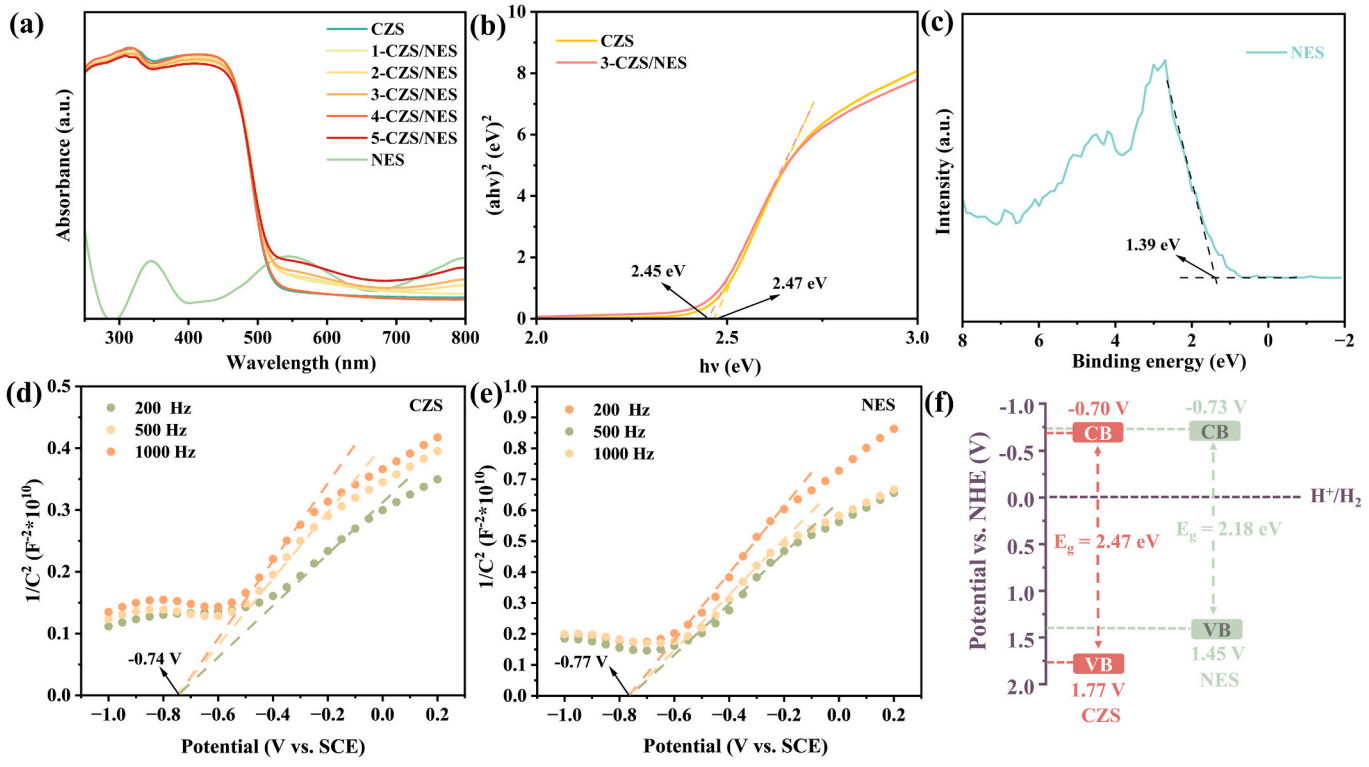

Fig. 3. (a) UV–Vis DRS spectra of CZS, NES and x-CZS/NES (x = 1, 2, 3, 4, and 5). (b) Tauc plots of CZS and 3-CZS/NES. (c) VB-XPS spectrum of NES. Mott–Schottky curves of (d) CZS and (e) NES recorded at 200, 500, and 1000 Hz. (f) Illustration of energy band positions of CZS and NES.

long-pass filter, using Na_2S/Na_2SO_3 as sacrificial agents. To examine the effect of sacrificial agent concentration on H_2 evolution, the Na_2S/Na_2SO_3 concentration was varied while maintaining a fixed molar ratio (Fig. S8, Table S2). The H_2 evolution activity increased markedly at relatively low sacrificial agent concentrations and gradually approached a plateau at 100% and higher concentrations. This behavior can be attributed to increasingly efficient hole consumption and suppressed charge recombination with increasing Na_2S/Na_2SO_3 concentration, whereas further increases provide only a limited additional benefit once hole scavenging becomes sufficiently effective. Therefore, 0.35 M Na_2S/0.25 M Na_2SO_3, which lies in the near-plateau region, was adopted as the standard sacrificial-agent system for subsequent hydrogen evolution measurements. The suspension pH changed only slightly from 13.48 before irradiation to 13.41 after the reaction, indicating that the strongly alkaline reaction environment remained relatively stable during photocatalysis. As shown in Fig. 4a, pristine CZS exhibits a PHE rate of 14.04 mmol·g^{-1}·h^{-1}, whereas pristine NES shows negligible activity. After the incorporation of NES, CZS/NES composites display significantly enhanced photocatalytic performance. By optimizing the NES content, 3-CZS/NES achieves the highest H_2 evolution rate of 46.53 mmol·g^{-1}·h^{-1}, approximately 3.3 times that of pristine CZS. To elucidate the role of NES in the CZS/NES heterojunction, control experiments were performed. As presented in Fig. 4b, 3-CZS/NES exhibits higher photocatalytic H_2 evolution activity than the physically mixed CZS-NES, CZS with free ethylenediamine, CZS with $NiCl_2$, and NiS-modified CZS. These results indicate that neither the free en ligand nor simple Ni-containing species alone can account for the superior activity of 3-CZS/NES, highlighting the important role of the bidentate-chelated NES coordination unit and its specific interfacial electronic coupling with CZS in promoting photocatalytic H_2 evolution. In addition, 3-CZS/NES outperforms 1 wt% Pt-loaded CZS and compares favorably with many reported CZS-based photocatalysts (Fig. 4e, Table S3), underscoring the effectiveness of this noble-metal-free design for photocatalytic hydrogen evolution. The durability of CZS and 3-CZS/NES was further examined through consecutive recycling tests (Fig. 4c and S9). Pristine CZS shows a gradual decline in activity, retaining only 74.0% of its initial H_2 evolution rate after four cycles, which can be attributed to the intrinsic photocorrosion of metal sulfide photocatalysts [8]. In contrast, 3-CZS/NES maintains 84.3% of its original activity under the same conditions, indicating improved photostability after coupling with NES. In addition, a 24 h continuous photocatalytic H_2 evolution experiment was conducted to assess the prolonged operational stability of 3-CZS/NES. As shown in Fig. S10, the cumulative hydrogen evolution increased nearly linearly throughout the irradiation period and reached 951.65 mmol·g^{-1} after 24 h, demonstrating sustained photocatalytic activity under prolonged irradiation. Inductively coupled plasma mass spectrometry (ICP-MS) analysis of the post-reaction solution after 24 h of irradiation revealed total amounts of Ni, Zn, and Cd of 1.50, 14.57, and 0.087 μg, respectively (Table S4), indicating limited leaching of the constituent metal species. The recovered 3-CZS/NES catalyst was subsequently characterized by TEM, XRD, FTIR, and XPS to assess its structural integrity after photocatalysis (Figs. S11–S15). The morphology, crystalline phases and surface chemical states show no appreciable changes after photocatalysis, confirming the structural integrity of the CZS/NES heterojunction during photocatalytic H_2 evolution [52]. The simultaneous enhancement in activity and durability suggests that NES serves not merely as an auxiliary component, but as a functional interfacial unit that favorably modulates the photocatalytic behavior of CZS. To quantitatively evaluate the photon-to-hydrogen conversion efficiency, the AQE values of 3-CZS/NES are summarized in Fig. 4d and Table S5. The experimental results reveal that the AQE of 3-CZS/NES reaches a maximum value of 18.6% under monochromatic

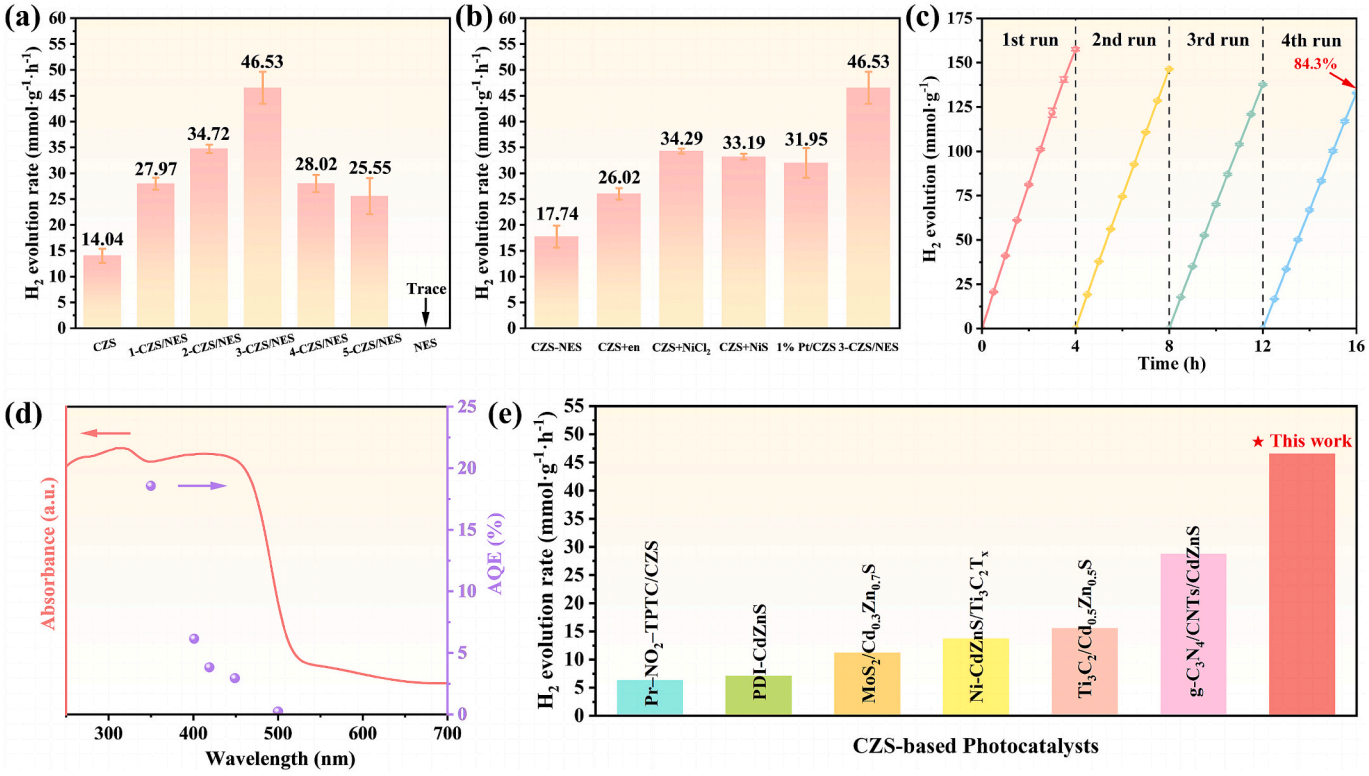

Fig. 4. (a) Photocatalytic hydrogen evolution rate (four replicates) of CZS, NES and x-CZS/NES (x = 1, 2, 3, 4, and 5). (b) Photocatalytic hydrogen evolution rate (four replicates) of CZS-NES, CZS + en, CZS + $NiCl_2$, CZS + NiS, 1% Pt/CZS and 3-CZS/NES. (c) Recycling photocatalytic hydrogen evolution tests (three replicates) of 3-CZS/NES. (d) UV–Vis DRS and wavelength-dependent AQE of 3-CZS/NES. (e) Comparison of photocatalytic hydrogen evolution activity of 3-CZS/NES with previously reported CZS-based photocatalysts, including Pr–NO_2–TPTC/CZS [54], PDI-CdZnS [55], $MoS_2/Cd_{0.3}Zn_{0.7}S$ [56], Ni-CdZnS/$Ti_3C_2T_x$ [57], $Ti_3C_2/Cd_{0.5}Zn_{0.5}S$ [58] and g-C_3N_4/CNTs/CdZnS [59].

irradiation at 350 nm. In addition, measurable AQEs of 3.8%, 2.9%, and 0.2% were obtained under monochromatic irradiation at 420, 450, and 500 nm, respectively, demonstrating that 3-CZS/NES remains photoactive across the visible-light range. Notably, the AQE trend follows the UV–Vis DRS spectrum closely, with the efficiency progressively decreasing as the excitation wavelength shifts toward the red end of the spectrum. This correlation confirms that H_2 evolution originates from photoinduced charge excitation and further supports the effective utilization of incident photons by the CZS/NES heterostructure [53].

To clarify the factors responsible for the superior photocatalytic activity of 3-CZS/NES, the charge-carrier dynamics were systematically investigated by photoelectrochemical and spectroscopic measurements. As shown in Fig. 5a, 3-CZS/NES produces a stronger transient photocurrent response than either CZS or NES, indicating more effective carrier extraction and interfacial transfer after heterojunction construction [60]. EIS measurements further support this conclusion. As shown in Fig. 5b, the Nyquist plot of 3-CZS/NES shows the smallest semicircle radius, suggesting lower interfacial charge-transfer resistance [61]. The relative ECSA was assessed using the double-layer capacitance (C_{dl}) derived from CV recorded within the non-Faradaic potential window (Fig. S16). The C_{dl} values of CZS, NES, and 3-CZS/NES were 13.16, 11.78, and 16.06 μF·cm^{-2}, respectively. The larger C_{dl} of 3-CZS/NES indicates increased electrochemically accessible surface area and available surface sites, which may facilitate the interfacial photocatalytic reactions [62,63]. Fig. 5c shows that 3-CZS/NES undergoes substantial PL quenching relative to pristine CZS. This quenching phenomenon is consistent with suppressed radiative electron–hole recombination and enhanced nonradiative interfacial charge transfer [64,65]. Time-resolved photoluminescence (TRPL) measurements further support this interpretation (Fig. 5d). The decay profiles were analyzed with a biexponential model, from which the average fluorescence lifetime (τ_{ave}) of 3-CZS/NES was determined to be 2.81 ns, which is shorter than that of pristine CZS (5.13 ns). The substantially shortened τ_1 after heterojunction formation is consistent with the introduction of an additional rapid interfacial charge-transfer pathway. The shortened lifetime, especially the greatly reduced fast component, supports accelerated carrier dynamics and interfacial charge transfer in the heterostructure [66]. These findings demonstrate that coupling CZS with NES effectively accelerates carrier separation and interfacial carrier transfer, which ultimately enhances the PHE performance.

3.3. *Experimental and theoretical elucidation of the S-scheme mechanism*

To probe the origin of the improved H_2 evolution performance of the CZS/NES heterojunction, UPS was performed using He I excitation ($h\nu = 21.22$ eV). According to $\Phi = h\nu - E_{cutoff}$, the work functions (Φ) of CZS, NES, and 3-CZS/NES were determined to be 3.76 eV, 3.48 eV, and 3.55 eV, respectively (Fig. 6a–c). Since the work function reflects the energetic separation between E_f and E_{vac}, a smaller Φ value indicates a higher E_f position [67]. Therefore, upon interfacial contact between CZS and NES, electrons spontaneously migrate from the NES (higher E_f) to CZS (lower E_f) until Fermi-level equilibration is reached. This spontaneous charge redistribution leads to electron enrichment on CZS and electron depletion on NES, thereby establishing an IEF across the

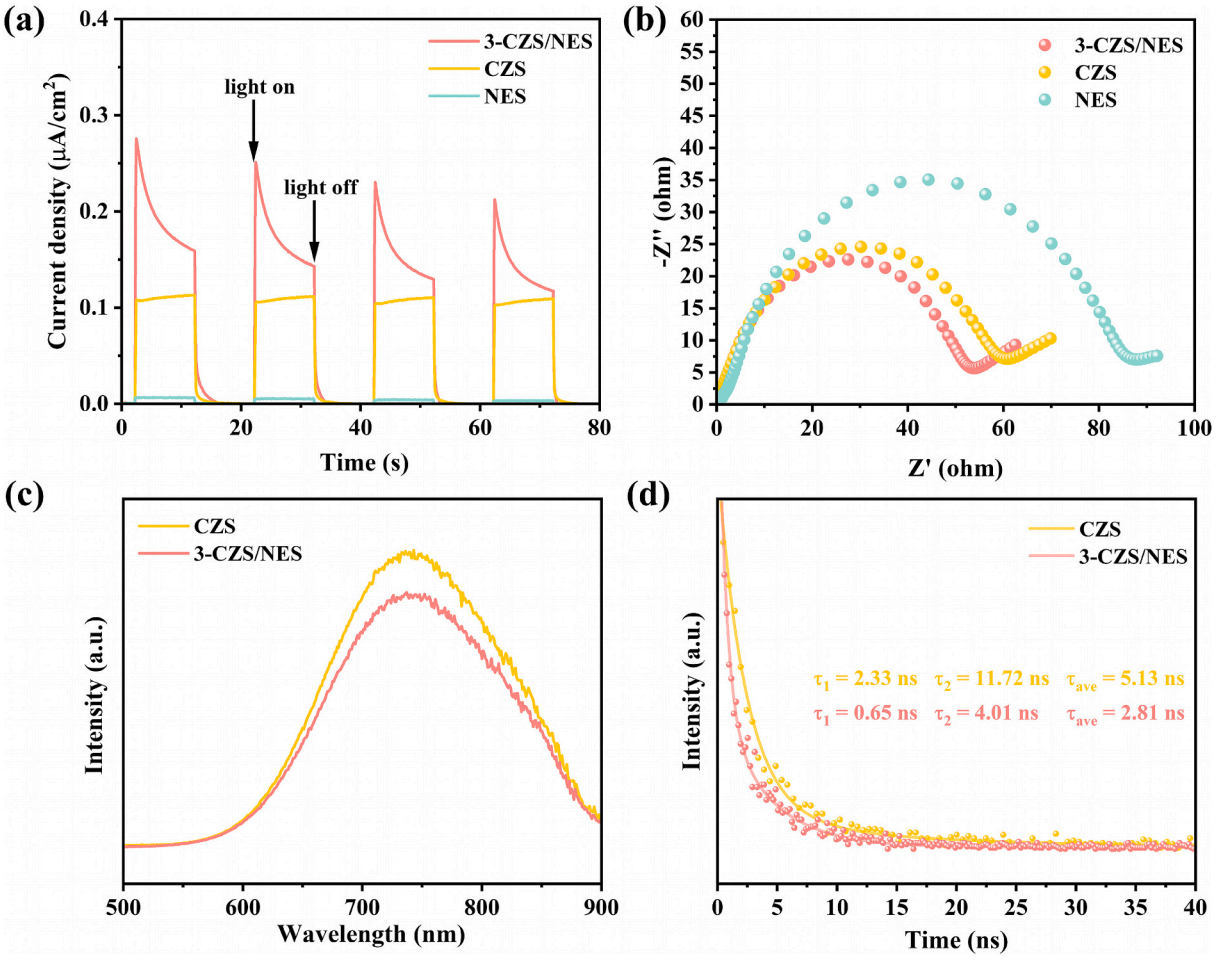

Fig. 5. (a) Transient photocurrent responses of CZS, NES, and 3-CZS/NES under intermittent light irradiation. (b) EIS Nyquist plots of CZS, NES, and 3-CZS/NES. (c) Steady-state PL emission spectra of CZS and 3-CZS/NES. (d) TRPL decay curves of CZS and 3-CZS/NES with an excitation wavelength of 380 nm.

interface oriented from NES toward CZS [68]. To further probe the light-induced charge-transfer pathway, ISI-XPS was subsequently employed. As shown in Fig. 6d–f, under illumination, the Cd 3d and Zn 2p peaks of 3-CZS/NES exhibit positive shifts of 0.1 eV compared with the dark state, whereas the Ni 2p peaks undergo an opposite shift of 0.1 eV. These observations indicate that photoexcited electrons in the CB of CZS migrate toward the heterointerface, where they recombine with holes in the VB of NES. Such an interfacial recombination process agrees well with the S-scheme mechanism. To further verify the spatial distribution of photogenerated electrons, selective photodeposition experiments were performed. As shown in Fig. S17, the photodeposited Au species are distributed preferentially in the NES region of the CZS/NES heterostructure. Since Au deposition requires photoexcited electrons to reduce the Au precursor, this result suggests the accumulation of electrons on the NES side. EPR spectroscopy was employed to evaluate the redox capability of the photogenerated carriers. Fig. S18 shows that no obvious $\bullet O_2^-$ signals were observed for either CZS or 3-CZS/NES under dark conditions. Upon light irradiation, 3-CZS/NES exhibited a stronger $\bullet O_2^-$ signal than pristine CZS, indicating more effective utilization of photogenerated electrons with sufficient reduction ability after heterojunction formation. On the basis of these results, the proposed photocatalytic pathway is schematically depicted in Fig. 6g. Owing to the higher E_f of NES relative to CZS, spontaneous electron transfer from NES to CZS occurs upon heterojunction formation until Fermi level equilibration is reached. This interfacial electron redistribution gives rise to band bending and establishes an IEF directed from NES toward CZS. Under visible-light irradiation, both CZS and NES are photoexcited, producing nonequilibrium charge carriers. The relatively low-energy electrons in the CB of CZS are driven toward the heterointerface, where they recombine with holes in the VB of NES. Consequently, electrons with strong reduction capability remain in the CB of NES for proton reduction, while holes are preserved in the VB of CZS for sacrificial-agent oxidation. Such an S-scheme transfer route facilitates effective carrier separation while preserving the strong redox abilities of

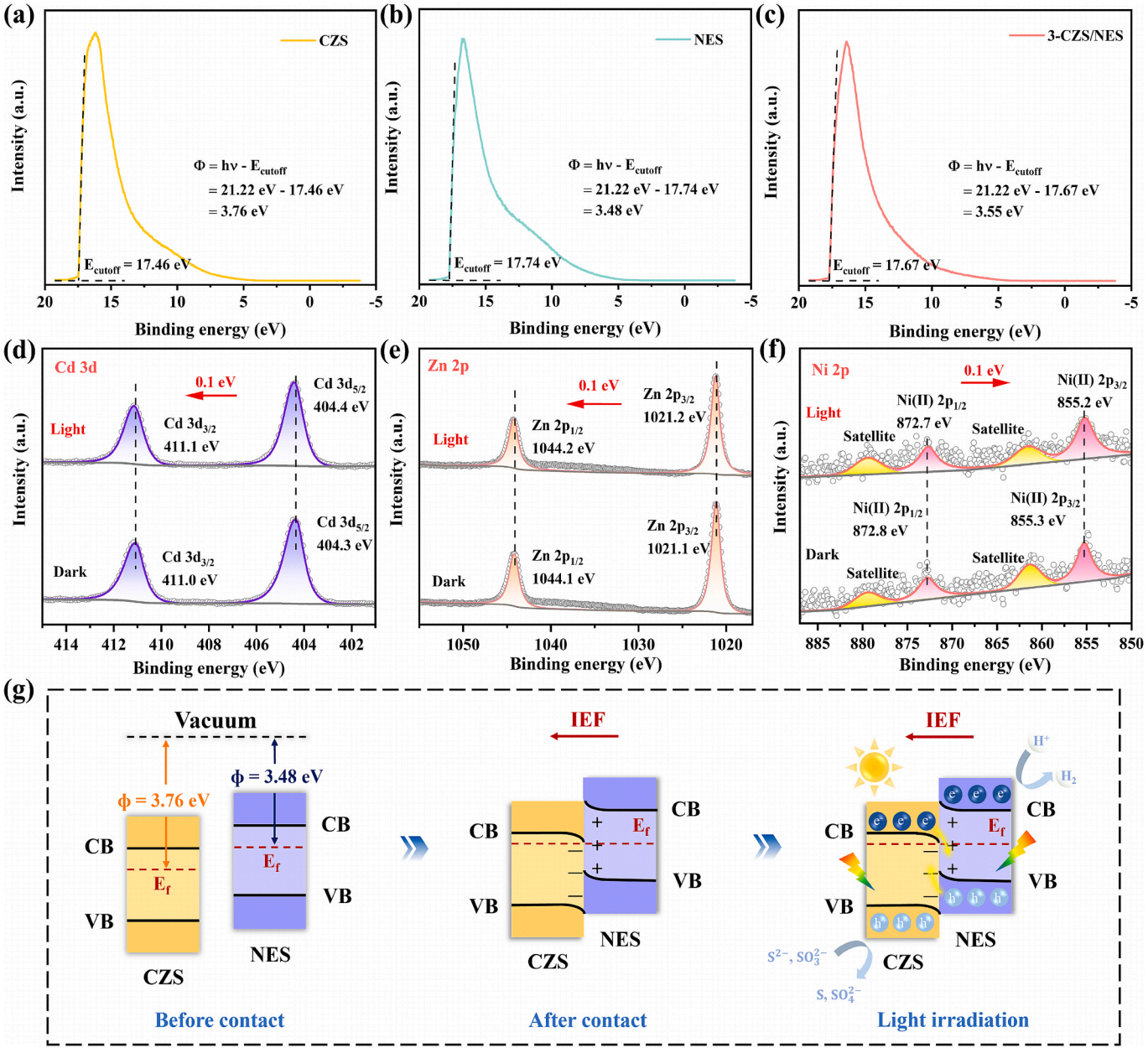

Fig. 6. UPS spectra of (a) CZS, (b) NES, and (c) 3-CZS/NES measured using He I excitation ($h\nu = 21.22$ eV). ISI-XPS spectra of 3-CZS/NES under dark and light irradiation conditions: (d) Cd 3d, (e) Zn 2p and (f) Ni 2p. (g) Schematic illustration of the proposed S-scheme mechanism in the CZS/NES heterojunction.

both components, which contributes to the superior PHE performance of the CZS/NES heterojunction.

To resolve the ultrafast charge-transfer behavior at the CZS/NES interface, fs-TAS was performed. As shown in the two-dimensional pseudocolor plots (Fig. 7a,d), following excitation by a 380 nm pump pulse, both CZS and 3-CZS/NES exhibit a prominent negative transient absorption band in the 520–750 nm region. This spectral signature is assigned to the ground state bleaching (GSB) associated with the CZS absorption [58]. The corresponding transient spectra at representative delay times are presented in Fig. 7b,e. The kinetic traces reveal that the excited-state carrier dynamics occur predominantly on the picosecond timescale. Notably, the fs-TAS intensity of pristine CZS reaches its maximum at 1 ps and subsequently attenuates with increasing delay time. In contrast, the fs-TAS signal of 3-CZS/NES peaks earlier at 0.5 ps and undergoes a faster subsequent decay. This acceleration implies that the construction of the heterojunction interface profoundly alters the excited-state carrier dynamics and facilitates a much more rapid interfacial charge-transfer or depletion process. The kinetic decay curves extracted at the GSB maximum (580 nm) were fitted using a multi-exponential function, with the detailed parameters summarized in Table S6. Pristine CZS can be reasonably described by a biexponential decay, consisting of a fast component for the excited-state relaxation of carriers ($\tau_1 = 41.8$ ps) and a long-lived component corresponding to the bulk exciton recombination ($\tau_2 = 5510$ ps) (Fig. 7c). Conversely, the carrier dynamics of 3-CZS/NES are markedly changed after hybridization. Most importantly, an additional ultrafast component ($\tau_3 = 5.96$ ps) emerges in the fitted kinetics, indicating the presence of a new ultrafast interfacial charge-transfer channel in the heterostructure [69] (Fig. 7f). This picosecond-scale process can be reasonably assigned to rapid carrier redistribution across the tightly contacted CZS/NES interface. Consequently, these findings provide dynamic spectroscopic evidence supporting the proposed S-scheme charge-transfer pathway.

DFT calculations were carried out to elucidate the atomic-scale electronic origin of the enhanced catalytic activity and interfacial carrier behavior in the CZS/NES heterojunction. Optimized structural models of CZS, NES, and the CZS/NES heterojunction are illustrated in Fig. S19. Considering the structural asymmetry of the surface terminations along the z-axis, the models exhibit distinct local work functions on opposite surfaces. Therefore, the work functions at the actual contact interfaces were extracted to evaluate the thermodynamic tendency of interfacial electron transfer. As shown in Fig. 8a,b, the calculated work functions at the contact surfaces of CZS and NES are 4.04 eV and 3.51 eV, respectively. This theoretical trend is in agreement with the UPS results, corroborating the higher Fermi-level position of NES relative to CZS. Accordingly, upon interfacial contact, electrons are expected to spontaneously migrate from the NES side to the CZS side. To visualize the spatial redistribution of charge at the interface, the charge density difference (CDD) was plotted, as shown in Fig. 8c. The cyan and yellow isosurfaces represent the electron depletion and accumulation zones, respectively. Electron depletion is mainly located on the NES side, whereas electron accumulation is concentrated near the CZS surface, further confirming the directional electron transfer from NES to CZS after heterojunction formation [70]. Furthermore, density of states (DOS) analysis reveals the electronic-structure modulation induced by heterojunction formation. As shown in Fig. 8d, pristine CZS exhibits a distinct bandgap region near the Fermi level, which is characteristic of a typical semiconductor. In contrast, NES shows pronounced Ni 3d contributions in the valence band region, accompanied by the participation of ligand-related N 2p and O 2p orbitals (Fig. 8e). This indicates that its electronic structure is jointly governed by the coordinated Ni center and the surrounding ligand environment. Following heterojunction formation, the DOS of CZS/NES undergoes an evident reconstruction relative to the individual components (Fig. 8f). On the one hand, the introduction of NES induces a slight bandgap narrowing in CZS, thereby favoring a broader optical response range of the system. On the other hand, the distribution of the Ni 3d orbitals and the band-edge electronic states near the Fermi level are significantly modified, together with obvious overlap among Cd-, Zn-, Ni-, N-, and O-related states. This result demonstrates the existence of pronounced electronic coupling at the heterointerface, rather than a mere physical superposition of the two

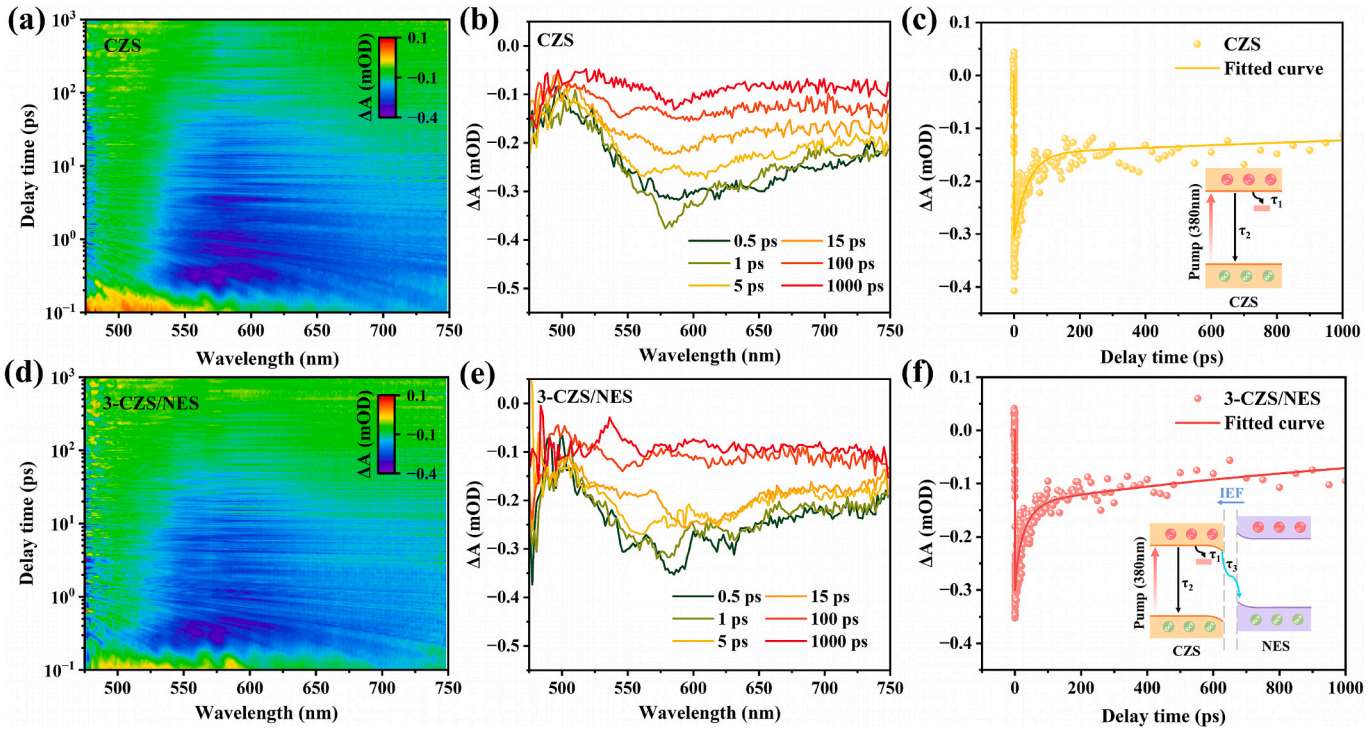

Fig. 7. Two-dimensional pseudocolor fs-TAS plots of (a) CZS and (d) 3-CZS/NES. Transient absorption spectra at selected probe delay times of (b) CZS and (e) 3-CZS/NES. Kinetic traces extracted at 580 nm and the corresponding multiexponential fitting curves for (c) CZS and (f) 3-CZS/NES. The insets schematically illustrate the carrier-relaxation and interfacial charge-transfer processes derived from the kinetic analysis.

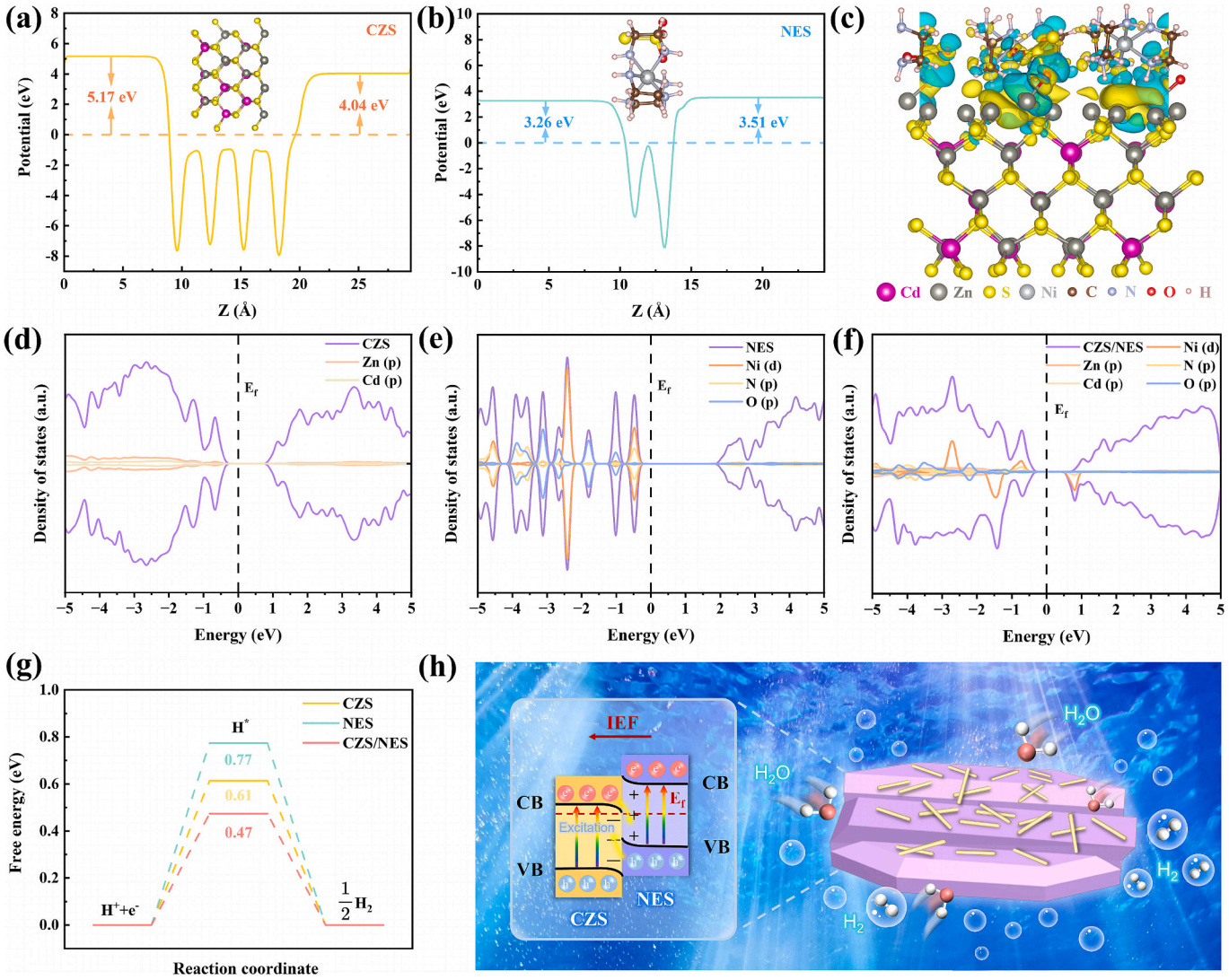

Fig. 8. The calculated electrostatic potentials of (a) CZS and (b) NES. (c) CDD of CZS/NES, where the yellow and cyan isosurfaces represent electron accumulation and depletion, respectively. Calculated DOS of (d) CZS, (e) NES and (f) CZS/NES. (g) Calculated Gibbs free-energy profiles for hydrogen adsorption on CZS, NES, and CZS/NES. (h) Schematic illustration of the proposed photocatalytic hydrogen evolution mechanism of the CZS/NES S-scheme heterojunction. (For interpretation of the references to colour in this figure legend, the reader is referred to the web version of this article.)

components. Such electronic state reconstruction facilitates interfacial charge redistribution and provides an electronic-structure basis for the proposed S-scheme route. In addition, the Gibbs free energy of hydrogen adsorption (ΔG_{H^*}) was calculated to evaluate the hydrogen evolution thermodynamics of the catalysts (Fig. 8g) and the corresponding H adsorption sites are illustrated in Fig. S20. In general, an ideal hydrogen evolution reaction (HER) catalyst should have a nearly thermoneutral hydrogen adsorption free energy, namely $\Delta G_{H^*} \approx 0$ eV [71,72]. The calculated ΔG_{H^*} values of pristine CZS and NES are 0.61 and 0.77 eV, respectively, indicating relatively weak H* adsorption, which is unfavorable for the HER kinetics. By comparison, the ΔG_{H^*} value of the CZS/NES heterojunction is reduced to 0.47 eV, indicating that interfacial coupling modifies the electronic character of the surface sites and renders H adsorption thermodynamically more favorable, thereby facilitating the surface hydrogen-evolution process. Combined with the above experimental results, these calculations suggest that constructing the S-scheme heterojunction not only promotes the separation of carriers with strong redox capability but also synergistically optimizes the surface reaction thermodynamics, ultimately endowing CZS/NES with superior photocatalytic H_2 evolution performance.

On the basis of the above experimental and theoretical results, a plausible S-scheme photocatalytic H_2 evolution mechanism for the CZS/NES heterojunction is proposed, as illustrated in Fig. 8h. The introduction of the bidentate-chelated octahedral Ni complex NES not only modulates the electronic structure of CZS, broadening its light-harvesting capacity, but also improves the photostability of the system. More importantly, owing to the difference in Fermi levels between CZS and NES, a robust IEF directed from NES to CZS is established. Under visible light, both components are photoexcited, generating electrons in the CB and holes in the VB. Driven by the synergistic effects of the IEF and interfacial band bending, the low-energy electrons in the CB of CZS undergo ultrafast recombination with the holes in the VB of NES at the heterointerface. Consequently, the highly reductive electrons remaining in the CB of NES are effectively preserved for H_2 evolution, while the holes retained in the VB of CZS participate in the sacrificial oxidation reaction. Therefore, the CZS/NES heterojunction not only enables efficient spatial separation of charge carriers while preserving strong redox capability, but also synergistically optimizes interfacial charge-transfer kinetics and surface hydrogen-evolution thermodynamics, ultimately contributing to its superior photocatalytic H_2 evolution activity and stability.

4. Conclusions

In summary, we have established an S-scheme heterojunction by integrating $Cd_{0.3}Zn_{0.7}S$ (CZS) with the chelation-stabilized octahedral Ni complex $[Ni(en)_3]S_2O_3$ (NES). Previous photocatalytic systems have mainly relied on coupling CZS with conventional semiconductors or cocatalysts to regulate interfacial charge transfer [55,69]. In contrast, this work introduces a Ni coordination complex as an intrinsic interfacial electronic regulator, extending S-scheme interface design toward coordination-complex-mediated electronic regulation. Beyond serving as a structural additive, NES acts as a functional interfacial electronic unit that regulates the electronic structure of CZS, broadens light harvesting, and improves photostability. The optimized 3-CZS/NES exhibits a superior H_2 evolution rate of 46.53 $mmol \cdot g^{-1} \cdot h^{-1}$, outperforming pristine CZS by a factor of 3.3 and remarkably surpassing Pt-loaded CZS under the same conditions. Although noble metal cocatalysts are highly effective in promoting photocatalytic hydrogen evolution, their limited abundance and high cost restrict their practical application [13]. This work offers an earth-abundant, noble-metal-free alternative while retaining high photocatalytic activity. Notably, this activity markedly exceeds those of representative CZS-based photocatalysts reported [57–59], highlighting the effectiveness of coordination-complex-mediated interface engineering. Control experiments further show that free ethylenediamine, simple Ni species, ligand-free NiS, or physical mixing of CZS and NES cannot reproduce the activity of the in situ constructed heterojunction, underscoring the importance of the retained NES coordination unit and its specific interfacial coupling with CZS. Compared with previous S-scheme studies [63], this work establishes a more comprehensive mechanistic framework by integrating ultraviolet photoelectron spectroscopy (UPS), in situ irradiated X-ray photoelectron spectroscopy (ISI-XPS), selective photodeposition, electron paramagnetic resonance (EPR), femtosecond transient absorption spectroscopy (fs-TAS), and density functional theory (DFT) calculations to elucidate interfacial charge transfer from energetic, spatial, redox, dynamic, and theoretical perspectives. Mechanistically, UPS, ISI-XPS, selective photodeposition and EPR reveal spontaneous electron redistribution from NES to CZS upon heterojunction formation, resulting in interfacial band bending and a built-in electric field favorable for S-scheme charge transfer. Ultrafast spectroscopy directly reveals a picosecond interfacial charge-redistribution process, whereas DFT calculations corroborate that the heterojunction formation profoundly restructures the interfacial electronic coupling and renders hydrogen adsorption thermodynamically more favorable. This work demonstrates the potential of chelation-stabilized transition-metal complexes as a new class of programmable interfacial regulators for photocatalytic systems. Future studies could focus on systematically tuning the metal centers, ligand fields, coordination geometries, and counterions to establish quantitative structure–interface–activity relationships, while further improving the chemical durability of such coordination interfaces and extending this strategy toward more practical photocatalytic systems with reduced dependence on sacrificial reagents. Therefore, this study not only provides a promising route toward efficient and noble-metal-free S-scheme photocatalysts, but also provides a broader strategy for coordination-chemistry-guided interface engineering in solar energy conversion.

CRediT authorship contribution statement

Yifan Liao: Writing – original draft, Validation, Methodology, Investigation, Conceptualization. **Jiayi Meng:** Writing – review & editing. **Quanmei Zhou:** Validation, Formal analysis. **Yuchen Wei:** Validation. **Yuying Hu:** Formal analysis. **Mohan Zhang:** Validation. **Yakun Song:** Writing – review & editing. **Bite Deng:** Formal analysis. **Hongyan Zhao:** Validation. **Wei-Lin Dai:** Writing – review & editing, Visualization, Supervision, Project administration, Funding acquisition.

Declaration of competing interest

The authors declare that they have no known competing financial interests or personal relationships that could have appeared to influence the work reported in this paper.

Acknowledgements

This work was financially supported by the National Key Research and Development Program of China (2021YFA1501404), and the Science and Technology Commission of Shanghai Municipality (2024ZDSYS02).

Appendix A. Supplementary data

Supplementary data to this article can be found online at https://doi.org/10.1016/j.jcis.2026.141794.

Data availability

Data will be made available on request.

References

[1] H. Song, S. Luo, H. Huang, B. Deng, J. Ye, Solar-driven hydrogen production: recent advances, challenges, and future perspectives, ACS Energy Lett. 7 (2022) 1043–1065.
[2] J. Corredor, M.J. Rivero, C.M. Rangel, F. Gloaguen, I. Ortiz, Comprehensive review and future perspectives on the photocatalytic hydrogen production, J. Chem. Technol. Biotechnol. 94 (2019) 3049–3063.
[3] K. Nath, M.M. Najafpour, R.A. Voloshin, S.E. Balaghi, E. Tyystjärvi, R. Timilsina, J. J. Eaton-Rye, T. Tomo, H.G. Nam, H. Nishihara, S. Ramakrishna, J.R. Shen, S. I. Allakhverdiev, Photobiological hydrogen production and artificial photosynthesis for clean energy: from bio to nanotechnologies, Photosynth. Res. 126 (2015) 237–247.
[4] J. Li, C. Jin, Y. Zhao, X. Yu, W. Ren, L. Sun, L. Wang, W. Wang, J. Zhang, J. Yang, Q. Liu, Selective hydrogen production enabled by WN plasmon-mediated formic acid adsorption reconfiguration, ACS Catal. 15 (2025) 12123–12132.
[5] W. Li, C. Cheng, J. Zhao, Y. Song, C. Xue, Enhanced azo dye removal through sequential ultrasound-assisted-treatment and photocatalysis using CdZnS, Angew. Chem. Int. Ed. 64 (2025) e202425508.
[6] X. Zhang, G. Yang, C. Han, J. Yang, Z. Zeng, Z. Xiong, J. Jia, K. Sa, H. Ye, Y. Liang, Construction of 0D/2D CdZnS quantum dots/$SnIn_4S_8$ nanosheets heterojunction photocatalysts for boosting photocatalytic performance, Colloids Surf. A Physicochem. Eng. Asp. 664 (2023) 131184.
[7] Z. Wang, D. Lu, K.K. Kondamareddy, Y. He, W. Gu, J. Li, H. Fan, H. Wang, W. Ho, Recent advances and insights in designing $Zn_xCd_{1-x}S$-based photocatalysts for hydrogen production and synergistic selective oxidation to value-added chemical production, ACS Appl. Mater. Interfaces 16 (2024) 48895–48926.
[8] W. Shao, Y. Hu, W. Chen, H. Zhao, J. Zhang, Y. Xie, L. Wang, F. Zhang, X. Chen, C. Cao, Y. Li, W. Song, $NiSe_2$/GDY/Sv-CdZnS dual S-scheme heterojunction boosts full-spectrum photocatalytic hydrogen evolution via synergistic ladder-like built-in electric field and photothermal effects, Adv. Funct. Mater. 36 (2026) e22964.
[9] Q. Hu, H. Yin, Y. Liu, A. Ablez, Z. Wang, Y. Zhan, C. Du, X. Huang, Tailoring the morphology and charge transfer pathways of ultrathin $Cd_{0.8}Zn_{0.2}S$ nanosheets via ionic liquid-modified Ti_3C_2 MXenes towards remarkable photocatalytic hydrogen evolution, J. Mater. Sci. Technol. 204 (2025) 47–59.
[10] K. Yu, T. Zhang, Y. Wang, J. Wu, H. Huang, K. Yin, F. Liao, Y. Liu, Z. Kang, Anchoring Co_3O_4 on CdZnS to accelerate hole migration for highly stable photocatalytic overall water splitting, Appl. Catal. Environ. 324 (2023) 122228.
[11] B. Weng, M.-Y. Qi, C. Han, Z.-R. Tang, Y.-J. Xu, Photocorrosion inhibition of semiconductor-based photocatalysts: Basic principle, current development, and future perspective, ACS Catal. 9 (2019) 4642–4687.
[12] Y. Liu, Z. Sun, Y.H. Hu, Bimetallic cocatalysts for photocatalytic hydrogen production from water, Chem. Eng. J. 409 (2021) 128250.
[13] B. Li, C. Guo, X. Wang, W. Dong, B. Xu, X. Xing, D. Zhou, X. Xue, Q. Luan, W. Tang, C. Hou, Strong interaction of single-atom Pt with $Cd_{0.5}Zn_{0.5}S$: Electronic structure regulation and photocatalytic hydrogen evolution promotion, Mater. Today Nano 21 (2023) 100281.
[14] H. Chen, K. Ye, W. Zhang, L. Fan, F. Kong, R. Zhao, M. Chen, Nickel-based bifunctional cocatalyst to enhance CdS photocatalytic hydrogen production, Langmuir 39 (2023) 18935–18945.
[15] Z. Cheng, W. Qi, C.H. Pang, T. Thomas, T. Wu, S. Liu, M. Yang, Recent advances in transition metal nitride-based materials for photocatalytic applications, Adv. Funct. Mater. 31 (2021) 2100553.
[16] H. Jiang, J. Li, X. Yu, H. Dong, W. Wang, Q. Liu, Interface engineering of covalent β-ketoenamine-bridged S-scheme heterojunction for synergistic solar-powered CO_2-to-CO conversion paired with selective alcohol oxidation, Chin. J. Catal. 80 (2026) 113–122.

[17] H. Qin, L. Wang, Y. Tang, W. Shi, C. Lu, Modulating charge kinetics in CDs/CTF S-scheme hybrids for enhanced H_2O_2 photosynthesis, Chin. J. Struct. Chem. 45 (2026) 100858.

[18] P. Hao, P. Shan, X. Wang, B. Xiong, L. Wang, J. Hou, C. Lu, Q. Yan, C. Li, W. Shi, Ni-Co Prussian blue analogues with tunable defects as heat-core materials for achieving ultra-high photothermal-assisted photocatalytic H_2 production, Renew. Energy 256 (2026) 124159.

[19] Q. Xu, L. Zhang, B. Cheng, J. Fan, J. Yu, S-scheme heterojunction photocatalyst, Chem 6 (2020) 1543–1559.

[20] T. Li, N. Tsubaki, Z. Jin, S-scheme heterojunction in photocatalytic hydrogen production, J. Mater. Sci. Technol. 169 (2024) 82–104.

[21] A. Kumar, A. Khosla, S. Kumar Sharma, P. Dhiman, G. Sharma, L. Gnanasekaran, M. Naushad, F.J. Stadler, A review on S-scheme and dual S-scheme heterojunctions for photocatalytic hydrogen evolution, water detoxification and CO_2 reduction, Fuel 333 (2023) 126267.

[22] Z. Meng, S. Chen, P. Yang, Y. Yan, G. Jiang, Q. Zhang, Y. Li, G-C_3N_4-based S-scheme heterojunction photocatalyst and its application, Chin. J. Struct. Chem. 45 (2026) 100889.

[23] B.J. McNicholas, Z.J. Tong, D. Bím, R.F. Turro, N.P. Kazmierczak, J. Chalupský, S. E. Reisman, R.G. Hadt, Electronic structures of nickel(II)-bis(indanyloxazoline)-dihalide catalysts: Understanding ligand field contributions that promote C(sp^2)–C(sp^3) cross-coupling, Inorg. Chem. 62 (2023) 14010–14027.

[24] Z. Wang, W. Sun, G. Li, Y. Li, B. Jiang, Nickel-based photocatalyst: from structure to application, ACS Appl. Mater. Interfaces 17 (2025) 41457–41497.

[25] J.-W. Wang, W.-J. Liu, D.-C. Zhong, T.-B. Lu, Nickel complexes as molecular catalysts for water splitting and CO_2 reduction, Coord. Chem. Rev. 378 (2019) 237–261.

[26] K.J. Nelson, N.P. Kazmierczak, D.A. Cagan, A.H. Follmer, T.R. Scott, S.L. Raj, D. Garratt, N. Powers-Riggs, K.J. Gaffney, R.G. Hadt, A.A. Cordones, Multiconfigurational electronic structure of nickel cross-coupling catalysts revealed by X-ray absorption spectroscopy, J. Phys. Chem. Lett. 16 (2025) 87–94.

[27] S. Deolka, R. Govindarajan, E. Khaskin, R.R. Fayzullin, M.C. Roy, J. R. Khusnutdinova, Photoinduced trifluoromethylation of arenes and heteroarenes catalyzed by high-valent nickel complexes, Angew. Chem. Int. Ed. 60 (2021) 24620–24629.

[28] M.L. Helm, M.P. Stewart, R.M. Bullock, M.R. DuBois, D.L. DuBois, A synthetic nickel electrocatalyst with a turnover frequency above 100,000 s^{-1} for H_2 production, Science 333 (2011) 863–866.

[29] Q.-X. Peng, D. Xue, S.-Z. Zhan, C.-L. Ni, Visible-light-driven photocatalytic system based on a nickel complex over CdS materials for hydrogen production from water, Appl. Catal. B Environ. 219 (2017) 353–361.

[30] Y. Wei, S.-X. Liu, H. Mueller-Bunz, M. Albrecht, Synthesis of triazolylidene nickel complexes and their catalytic application in selective aldehyde hydrosilylation, ACS Catal. 6 (2016) 8192–8200.

[31] C. Tao, C. Lu, W. Lu, J. Wen, C. Wang, G. Huang, Synthesis of tris(ethylenediamine) nickel(II) thiosulfate [Ni(en)$_3$S$_2$O$_3$] for efficient electrocatalytic hydrogen evolution, Mater. Lett. 330 (2023) 133343.

[32] G. Kresse, J. Furthmüller, Efficiency of ab-initio total energy calculations for metals and semiconductors using a plane-wave basis set, Comput. Mater. Sci. 6 (1996) 15–50.

[33] J.P. Perdew, K. Burke, M. Ernzerhof, Generalized gradient approximation made simple, Phys. Rev. Lett. 77 (1996) 3865–3868.

[34] S. Grimme, J. Antony, S. Ehrlich, H. Krieg, A consistent and accurate ab initio parametrization of density functional dispersion correction (DFT-D) for the 94 elements H-Pu, J. Chem. Phys. 132 (2010) 154104.

[35] G. Kresse, D. Joubert, From ultrasoft pseudopotentials to the projector augmented-wave method, Phys. Rev. B 59 (1999) 1758–1775.

[36] H.J. Monkhorst, J.D. Pack, Special points for Brillouin-zone integrations, Phys. Rev. B 13 (1976) 5188–5192.

[37] K.M. Ho, C.L. Fu, B.N. Harmon, W. Weber, D.R. Hamann, Vibrational frequencies and structural properties of transition metals via total-energy calculations, Phys. Rev. Lett. 49 (1982) 673–676.

[38] X. Wang, L. Li, H. Gu, H. Zhang, J. Zhang, Q. Zhang, W.-L. Dai, Highly efficient noble-metal-free NiS/rGO/$Cd_{0.3}Zn_{0.7}S$ nanorods in visible-light-driven H_2 evolution with enhanced surface photoinduced charge transfer, Appl. Surf. Sci. 574 (2022) 151553.

[39] N. Braidy, A. Béchu, J.C. de Souza Terra, G.S. Patience, Experimental methods in chemical engineering: Transmission electron microscopy—TEM, Can. J. Chem. Eng. 98 (2020) 628–641.

[40] G. Yellaiah, K. Hadasa, M. Nagabhushanam, Structural, optical and vibrational studies of Na^+ doped $Cd_{0.8}Zn_{0.2}S$ semiconductor compounds, J. Alloys Compd. 581 (2013) 805–811.

[41] V.N. Pham, S. Lee, H. Lee, H.S. Kim, Revealing photocatalytic performance of $Zn_xCd_{1-x}S$ nanoparticles depending on the irradiation wavelength, Inorg. Chem. 62 (2023) 3703–3711.

[42] N. Noorani, H. Rahemi, S.F. Tayyari, Conformational stabilities, EPR, IR and VCD studies of tris(ethylenediamine)nickel(II) chloride, J. Iran. Chem. Soc. 7 (2010) 934–945.

[43] M. Thommes, K. Kaneko, A.V. Neimark, J.P. Olivier, F. Rodriguez-Reinoso, J. Rouquerol, K.S.W. Sing, Physisorption of gases, with special reference to the evaluation of surface area and pore size distribution, Pure Appl. Chem. 87 (2015) 1051–1069.

[44] L. Liu, W. Zhao, T. Gao, E. Liu, H. Ma, T. Sun, $CoSe_2$/$MoSe_2$ heterojunction as an efficient electrocatalyst for energy-saving hydrogen production and electro-treatment of organic molecules, Materials Today Chemistry 48 (2025) 103000.

[45] D. Yan, H. Miao, J. Fan, Q. Yu, E. Liu, T. Sun, Constructing dual cocatalysts of Ni_2P–NiS-decorated TiO_2 for boosting photocatalytic H_2 evolution, Langmuir 39 (2023) 16648–16656.

[46] A.P. Grosvenor, M.C. Biesinger, R.S.C. Smart, N.S. McIntyre, New interpretations of XPS spectra of nickel metal and oxides, Surf. Sci. 600 (2006) 1771–1779.

[47] F.A. Stevie, C.L. Donley, Introduction to X-ray photoelectron spectroscopy, J. Vac. Sci. Technol. A 38 (2020) 063204.

[48] G. Bussière, C. Reber, Coupled excited states in nickel(II) complexes probed by polarized absorption spectroscopy, J. Am. Chem. Soc. 120 (1998) 6306–6315.

[49] M. Zhou, Z. Yu, G. Yu, R. Fu, S. Wang, W. Yang, X. Liao, Y. Zhao, Z. Wang, Constructing of n-type semiconductor heterostructures for efficient hydrazine-assisted hydrogen production, Adv. Funct. Mater. 35 (2025) 2415058.

[50] E.A. Abdullah, Band edge positions as a key parameter to a systematic design of heterogeneous photocatalyst, Eur. J. Chem. 10 (2019) 82–94.

[51] T. Hisatomi, J. Kubota, K. Domen, Recent advances in semiconductors for photocatalytic and photoelectrochemical water splitting, Chem. Soc. Rev. 43 (2014) 7520–7535.

[52] Z. Zhao, J. Wu, Y.-Z. Zheng, N. Li, X. Li, Z. Ye, S. Lu, X. Tao, C. Chen, Stable hybrid perovskite $MAPb(I_{1-x}Br_x)_3$ for photocatalytic hydrogen evolution, Appl. Catal. B Environ. 253 (2019) 41–48.

[53] X. Shi, C. Dai, X. Wang, J. Hu, J. Zhang, L. Zheng, L. Mao, H. Zheng, M. Zhu, Protruding Pt single-sites on hexagonal $ZnIn_2S_4$ to accelerate photocatalytic hydrogen evolution, Nat. Commun. 13 (2022) 1287.

[54] T.-T. Li, Y. Chen, Y. Cheng, M.-Q. Zheng, J.-F. Qian, M.-Y. He, Q. Chen, Z.-H. Zhang, Synthesis of rare earth MOF/CZS materials derived from aromatic tetracarboxylic acids and photocatalytic hydrogen production, Int. J. Hydrogen Energy 65 (2024) 225–235.

[55] W. Cai, J. Liu, Z. Liao, Y. Luo, X. Xiang, B. Li, W. Yang, Y. Fang, Interface-engineered CdZnS/PDI S-scheme photocatalyst with synergistic effects for enhanced hydrogen production, J. Alloys Compd. 1037 (2025) 182463.

[56] J. Xing, Y. Wang, G. Shi, L. Li, Y. Wu, Defective $Cd_{0.3}Zn_{0.7}S$/1T-2H MoS_2 Z-scheme heterojunctions: Rational design with efficient charge transfer for enhanced photocatalytic H_2 generation, J. Alloys Compd. 988 (2024) 174302.

[57] C. Yuan, J. Li, Y. Zhuang, D. Guo, S. Meng, D. Zhang, X. Yang, G. Sui, Constructing a sulfure-vacancy enriched Schottky heterojunction in Ni-CdZnS/$Ti_3C_2T_x$ for efficient photocatalytic hydrogen evolution under visible light, Appl. Surf. Sci. 730 (2026) 166346.

[58] Q. Li, H. Zhang, H. Gu, Y. Cui, R. Gao, W.-L. Dai, In situ growth of $Cd_{0.5}Zn_{0.5}S$ nanorods on Ti_3C_2 MXene nanosheet for efficient visible-light-driven photocatalytic hydrogen evolution, Acta Phys.-Chim. Sin. 41 (2025) 100031.

[59] C. Feng, Z. Chen, J. Jing, M. Sun, J. Tian, G. Lu, L. Ma, X. Li, J. Hou, Significantly enhanced photocatalytic hydrogen production performance of g-C_3N_4/CNTs/CdZnS with carbon nanotubes as the electron mediators, J. Mater. Sci. Technol. 80 (2021) 75–83.

[60] X. Men, H. Chen, K. Chang, X. Fang, C. Wu, W. Qin, S. Yin, Three-dimensional free-standing ZnO/graphene composite foam for photocurrent generation and photocatalytic activity, Appl. Catal. B Environ. 187 (2016) 367–374.

[61] J. Pan, Z. Dong, B. Wang, Z. Jiang, C. Zhao, J. Wang, C. Song, Y. Zheng, C. Li, The enhancement of photocatalytic hydrogen production via Ti^{3+} self-doping black TiO_2/g-C_3N_4 hollow core-shell nano-heterojunction, Appl. Catal. B Environ. 242 (2019) 92–99.

[62] J. Tian, C. Guan, C. Liu, J. Fan, Y. Zhu, T. Sun, E. Liu, Double S-scheme $Cu_{2-x}Se$/twinned-$Cd_{0.5}Zn_{0.5}S$ homo-heterojunctions with surface plasmon effects for efficient photocatalytic H_2 evolution, J. Colloid Interface Sci. 666 (2024) 481–495.

[63] Z. Lei, W. Wang, T. Sun, E. Liu, T. Gao, Efficient photocatalytic H_2 evolution over SnS_2/twinned $Mn_{0.5}Cd_{0.5}S$ hetero-homojunction with double S-scheme charge transfer routes, J. Mater. Sci. Technol. 216 (2025) 81–92.

[64] Z. Bian, T. Tachikawa, W. Kim, W. Choi, T. Majima, Superior electron transport and photocatalytic abilities of metal-nanoparticle-loaded TiO_2 superstructures, J. Phys. Chem. C 116 (2012) 25444–25453.

[65] X. Shi, S. Kim, M. Fujitsuka, T. Majima, In situ observation of NiS nanoparticles depositing on single TiO_2 mesocrystal for enhanced photocatalytic hydrogen evolution activity, Appl. Catal. B Environ. 254 (2019) 594–600.

[66] X. Wang, H. Zhang, Y. Huang, L. Gao, Y. Zhang, J. Meng, Y. Liao, B. Zong, W.-L. Dai, H. Li, Nitrogen defects and interfacial chemical bonds in Fe single-site mediated C_3N_4 with rod-like Fe_2O_3 enhanced the S-scheme heterojunction for efficient energy conversion, Adv. Funct. Mater. (2025) 2421847.

[67] A. Kahn, Fermi level, work function and vacuum level, Mater. Horiz. 3 (2016) 7–10.

[68] M. Chen, J. Xiao, Y. Lei, X. Qin, S.K. Tiwari, N. Wang, Z. Wu, Y. Zhu, X. Wang, Strong internal electric field-driven S-scheme CoAl-LDH/ZrO_2 heterojunction for enhanced photocatalytic CO_2 reduction: Configuration, performance, and mechanism, Adv. Sci. 12 (2025) e10939.

[69] G. Sun, Z. Tai, J. Zhang, B. Cheng, H. Yu, J. Yu, Bifunctional g-C_3N_4 nanospheres/CdZnS QDs S-scheme photocatalyst with boosted H_2 evolution and furfural synthesis mechanism, Appl. Catal. B Environ. Energy 358 (2024) 124459.

[70] H. Gu, H. Zhang, X. Wang, Q. Li, S. Chang, Y. Huang, L. Gao, Y. Cui, R. Liu, W.-L. Dai, Robust construction of CdSe nanorods@Ti_3C_2 MXene nanosheet for superior photocatalytic H_2 evolution, Appl. Catal. Environ. 328 (2023) 122537.

[71] H. Liang, L. Wu, M.A. Rehan, D. Jin, G. Li, Dual-synergistic molybdenum disulfide and molybdenum carbide cocatalyst integrated with graphitic carbon nitride for efficient photocatalytic hydrogen production, J. Colloid Interface Sci. 702 (2026) 138926.

[72] J.K. Nørskov, T. Bligaard, A. Logadottir, J.R. Kitchin, J.G. Chen, S. Pandelov, U. Stimming, Trends in the exchange current for hydrogen evolution, J. Electrochem. Soc. 152 (2005) J23.